Effects of Ultrafast Laser Energy Deposition on a Hypervelocity Boundary Layer

Laurent M. Le Page,[1] Andrew Ceruzzi,[1] Thomas L. J. Brain,[2] Alexander J. Rieley,[2]

Tristan J. Crumpton,[1] James C. Robson,[2] Matthew Eckold,[2] and Matthew McGilvray[1]

Abstract

This paper presents a preliminary study of hypersonic boundary layer phenomena resulting from the energy deposition of an ultrafast laser pulse in proximity to the tip of a 7° half-angle axisymmetric cone within the Oxford High Density Tunnel (HDT) facility. An ultrafast Ti:Sapphire laser was integrated into the facility's systems, providing temporally precise and synchronous delivery of a single tightly focussed laser pulse to the target location in the HDT test section. This investigation independently assessed the variation of the freestream unit Reynolds number ($Re_{unit,\infty}$) on the disturbed boundary layer for laminar to turbulent conditions bound by the extrema unit Reynolds numbers 5.7 and $24.1 \pm 0.9 \times 10^6/m$, while keeping laser settings constant. For all test conditions, the boundary layer state was characterised using high-speed schlieren imaging at 1 MHz for visualising the flow field, focussed laser differential interferometry (FLDI) to assess small density fluctuations, and surface-mounted high-frequency bandwidth pressure transducers (PCBs 132A31 and 132B32). Flow features associated with the energy deposition in the boundary layer, included the formation of a spherical shock wave that expanded radially and decayed, an elliptical high-temperature 'hot spot' region, and a trailing turbulent wake. The hot spot and turbulent wake density gradients increased linearly with unit Reynolds number, suggesting a relation to the local mean density or pressure. Normalising these values by mean density gave an estimate of turbulence intensity, which appeared independent of unit Reynolds number. The size of the hot spot decreased with unit Reynolds number, which is hypothesised to be caused by the higher mean pressure compressing the hot spot. The increasing instability of the boundary layer with unit Reynolds number led to longer duration turbulent wakes before the laminar boundary layer re-establishes.

Keywords: *Boundary Layer, Hypersonic Flow, Ultrafast, Laser, High Energy, Shock Wave.*

Nomenclature

Latin

CAD – Computer Aided Design
CW – Continuous Wave
CWT – Continuous Wavelet Transform
HDT – High Density Tunnel
$H_{\Delta x}$ – Transfer Function of FLDI Foci Separation Length
H_w – Transfer Function of FLDI Laser Beam Radius at Focus
FLDI – Focussed Laser Differential Interferometry
FOV – Field of View
fs – Femtosecond

LIP – Laser-Induced Plasma
LGS – Laser Generated Shock
M^2 – Laser Beam Propagation Ratio
M_∞ – Mach Number
ns – Nanosecond
P_∞ – Freestream Pressure
$Re_{unit,\infty}$ – Unit Reynolds Number
T_∞ – Freestream Temperature
U_∞ – Freestream Velocity
UV – Ultraviolet
w_0 – FLDI Laser Beam Radius at Focus

Greek

[1]*University of Oxford, Department of Engineering Science, Parks Road, Oxford, OX1 3PJ. Corresponding author email address: laurent.lepage@eng.ox.ac.uk*
[2]*QinetiQ Limited, Cody Technology Park, Farnborough, Hampshire, GU14 0LX, United Kingdom*

Δx − FLDI Foci Separation Length
λ_0 − FLDI Laser Wavelength

λ_x − Flow Disturbance Wavelength
μ_∞ − Freestream Viscosity

1. Introduction

Energy deposition is a promising technique for flow control, drag reduction, and mixing enhancement on hypersonic bodies. An overview of the subject by Knight et al. [1] emphasised that, 'Significant research is needed to understand the effects of location, level and unsteady nature of energy deposition on the flow structure, and to develop optimal energy deposition (ED) schemes for specific aerodynamic applications.'

The potential applications of plasma-assisted flow modification via energy deposition can be classified into two main domains: (1) overseeing the primary flow, involving the manipulation of shock waves at high-speed conditions, and (2) controlling the boundary layer state. Primary flow changes include the modification of shock wave shapes, aerodynamic deceleration, and drag reduction. Boundary layer modification is further divided into managing laminar to turbulent transitions, preventing boundary layer separation, influencing lift and drag forces, as well as controlling acoustic perturbations and enhancing mixing efficiency [1, 2, 3] In comparison to alternative methods of depositing energy into a gas, which could be using microwave radiation, electron beams, or short high-voltage pulses, utilising a laser beam offers several advantages [2] [4]. It is electrodeless and surface-independent, allowing for precise targeting of high specific energy deposition. When a laser beam with sufficiently high energy density is focussed in a gaseous flow, the gas undergoes ionisation, forming a spark or plasma, which has been previously generated over a broad wavelength spectrum using various laser types [5]. The creation of a laser-induced plasma (LIP), from the absorption of laser beam energy by the gas molecular constituents, occurs when the beam is concentrated in a small focal volume, where its energy is large enough to librate electrons from their respective molecules, creating positively charged ions. This process unfolds through successive stages, starting with the generation of initial electrons through multiphoton ionisation, proceeding to avalanche ionisation in the focal region, absorption of laser energy by a gaseous plasma, rapid expansion of the plasma, and the formation of a shock wave that propagates into the surrounding gas [3, 6].

Klimov et al. conducted one of the pioneering investigations into the impact of plasma on the transmission of shock waves through a gas in the supersonic regime [7]. Their work recorded a rise in the shock wave's speed as it traversed through a gas discharge, accompanied by a concurrent reduction in the wave's magnitude. They compared this experimentally observed change in shock wave velocity with calculations that considered the energy discharged. The 400 m/s variance in anticipated shock speed was ascribed to potential gas heating due to processes such as vibrational quenching of molecules and the excitation of electronic states, alongside alterations in the geometry of the shock front. Advancements in femtosecond (fs) lasers have prompted recent work evaluating supersonic flow using slender plasma filaments formed during air breakdown from terawatt laser radiation lasting hundreds of fs [6, 7, 8].

Research into plasma-based flow modification for hypervelocity flows has explored various applications, such as mitigating bow shocks ahead of hemispherical models [9], truncated cone geometries [10], and in proximity to sharp-nosed axisymmetric cone models [11]. Notably, recent investigations have measured and visualised plasma effects on Mach 7 flow induced by a nanosecond (ns) laser pulse at the surface of a 7-degree cone model within the University of Oxford's High Density Tunnel (HDT), operating at a unit Reynolds number ($Re_{unit,\infty}$) of $12.3 \times 10^6/m$ [12]. This study involved creating plasma near the nose-tip of the cone, leading to the formation of a radially expanding spherical shock and a central hot gas region that expanded to a finite size. As these features moved downstream, the spherical shock expanded and interacted with the established body shock wave, while advection of the hot region left a finite length turbulent boundary layer in its path. Work presented here builds upon these findings by examining the impact of a fs or ultrafast laser pulse on a boundary layer using an identical cone model geometry across a range of unit Reynolds numbers within a Mach 7 flow.

2. Experimental Setup

2.1. Flow Facility & Conditions

Testing was carried out in the Oxford High Density Tunnel (HDT), a heated Ludwieg tube, which is schematically depicted in Figure 1 [13]. The HDT utilises an upstream-facing plug valve initially isolating the high-pressure 152 mm diameter and 17.35 m long barrel from the evacuated downstream section, the test section, and the dump tank. The barrel was heated to 500 K, and was operated at a maximum pressure of 26 bar. The Mach 7 nozzle used for this work has an exit diameter of 350 mm and produces a core flow of approximately 300 mm in diameter [14].
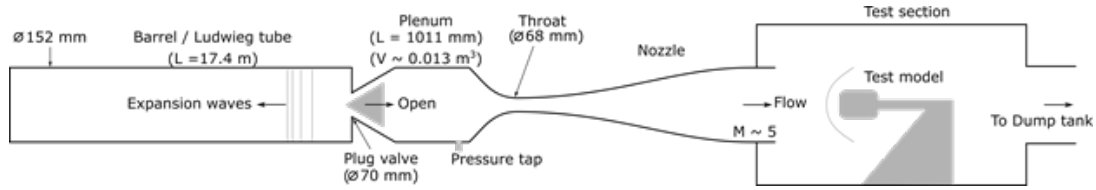
Fig 1. Schematic of the Oxford High-Density Tunnel (HDT)

To initiate experimental flow, fast acting valves vent the high-presses reservoir, causing the barrel pressure to overcome the plug valve, resulting in an abrupt release of heated, high pressure gas to enter the plenum, taking approximately 5 ms. As a result, upstream travelling expansion waves reflect from the upstream tunnel wall to return to the open downstream plug valve, entering the plenum. These expansion waves generate multiple steady-state test periods, referred to as plateaus, each exhibiting progressively lower total pressure values and typically last around 30 ms each. The total pressure of the test section is monitored upstream in the plenum by a Kulite XCQ-080 transducer with a range of 70 bar.

For the work presented here, four flow conditions at Mach 7 are used to assess the boundary layer state by varying the freestream unit Reynolds number from laminar to turbulent conditions spanning 5.7 to $24.1 \pm 0.9 \times 10^6/m$, which was achieved by adjusting the initial fill pressure of the Ludwieg tube barrel. Details of these flow conditions are listed in Table 1, where M_∞ is the Mach number, P_∞ the freestream pressure, T_∞ the freestream temperature, U_∞ the freestream velocity, and μ_∞ is the freestream viscosity, respectively.

Table 1. Investigated freestream conditions.

M_∞	Re_{unit}	P_∞	T_∞	U_∞	μ_∞
7 ± 0.35	$5.7 \pm 0.9 \times 10^6/m$	$230 \pm 25 Pa$	$42 \pm 3\ K$	$911 \pm 70\ m/s$	$3 \pm 2 \times 10^{-6}\ Pa\ s$
7 ± 0.35	$12.3 \pm 0.9 \times 10^6/m$	$490 \pm 25 Pa$	$42 \pm 3\ K$	$911 \pm 70\ m/s$	$3 \pm 2 \times 10^{-6}\ Pa\ s$
7 ± 0.35	$19.0 \pm 0.9 \times 10^6/m$	$760 \pm 25 Pa$	$42 \pm 3\ K$	$911 \pm 70\ m/s$	$3 \pm 2 \times 10^{-6}\ Pa\ s$
7 ± 0.35	$24.0 \pm 0.9 \times 10^6/m$	$960 \pm 25 Pa$	$42 \pm 3\ K$	$911 \pm 70\ m/s$	$3 \pm 2 \times 10^{-6}\ Pa\ s$

2.2. Test Model

A $7°$ half-angle axisymmetric cone with a base diameter of 146 mm and a total length of 594.5 mm (when a sharp nose tip is installed) was securely mounted in the HDT test section using a sting and an Angle of Attack (AoA) adjustable traverse that was set to 0° AoA. Figure 2 displays a 3D CAD model of the cone. The cone model was equipped with PCB 132B39 pressure transducers, mounted axially along the zeroth azimuth to monitor pressure fluctuation. Data from these on-board sensors was collected using a dedicated data acquisition system, sampling at 2 MHz, which is also used to synchronise facility operation with data capture.
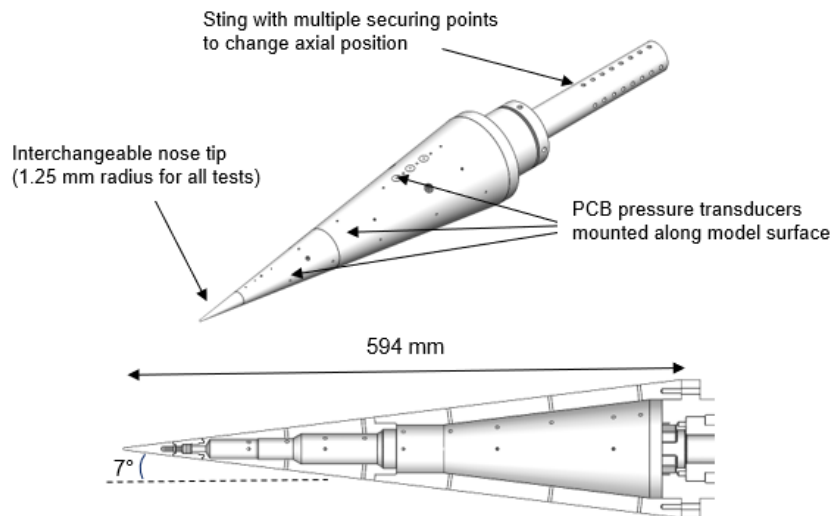
Fig 2. 7° axisymmetric cone model.

2.3. Integration of Ultrafast Laser System

These experiments used an Amplitude ARCO X 30 laser system, which operates at a repetition rate of 10 Hz and emits coherent monochromatic light at a central wavelength of 783 nm, with a beam propagation ratio (M^2) of 1.5, and an average power delivery of 400 mW. The nominal beam diameter of approximately 20 mm is focused to around 1 mm near the cone model's surface.

To align the optical path with the HDT test section, a pair of Thorlabs PL201 CW lasers (520 nm) were employed for mapping the path, which is illustrated in Figure 3. The fs laser system, housed in a separate room from the HDT facility, delivered the laser beam to the test section through a light-tight channel containing a turning mirror at an appropriate position. The mirror directed the beam to a periscope, elevating it from floor level to an optical table. Subsequently, the beam entered a conditioning and diagnostics enclosure mounted directly to the optical table adjacent to the HDT test section. Here, the energy and cross-sectional diameter of the beam were sampled and estimated. Exiting the enclosure, the beam traversed a periscope equipped with two ultrafast-enhanced silver mirrors. Following the periscope, the beam passed through an anti-reflection coated 50.8 mm diameter UV-fused silica window, serving as the interface to the test section. Inside the HDT test section, the beam propagated through a cage-mounted 300 mm plano-convex focusing lens to a final turning mirror. This mirror directed the converging beam toward the target region for the energy deposition.

3. Diagnostics

3.1. Schlieren Imaging

A schlieren system to visualise flow features was arranged in the z-type configuration and used a Cavitar Cavilux Smart UHS pulsed diode 640 nm laser for illumination; where images were taken by a Specialised Imaging - Kirana 5M high-speed camera with at a frame rate of 1 MHz. Pulsed illumination was reflected from the first parabolic mirror to the first planar mirror, through the HDT test section to the second planar mirror, which then sends the light to the final parabolic mirror, before being focussing the image over the knife edge, and into the camera [15, 16]. A simplified schematic of the schlieren arrangement together with FLDI, and the fs laser system is show in Figure 4.

To access both upstream and downstream fields-of-view (FOV), the light path and the cone model were translated accordingly. For example, the light path shifted downstream by altering the model position further upstream to view the downstream section of the cone model and its flow features. An example of the FOVs with this schlieren arrangement us shown below in Figure 5, which measure 159.22 and 151.18 mm, respectively.
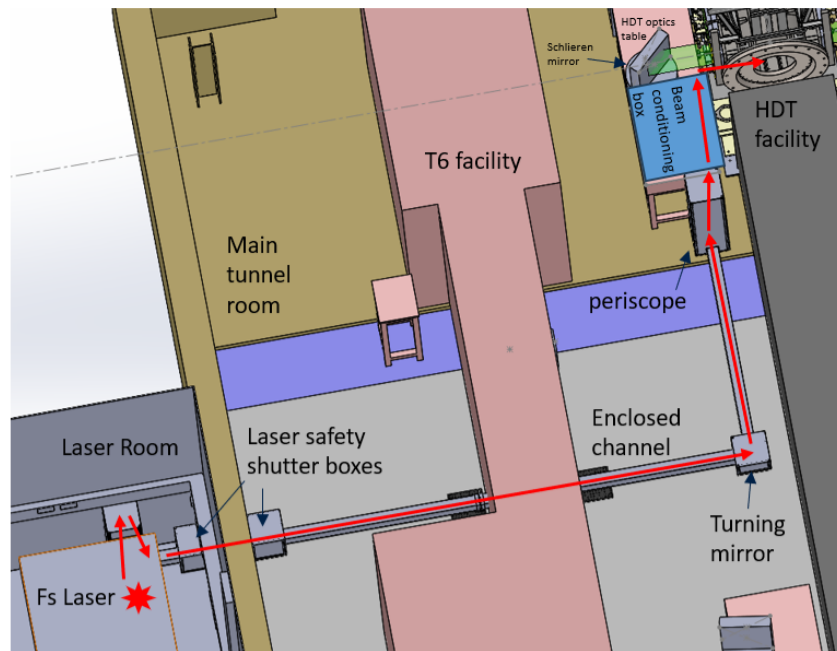
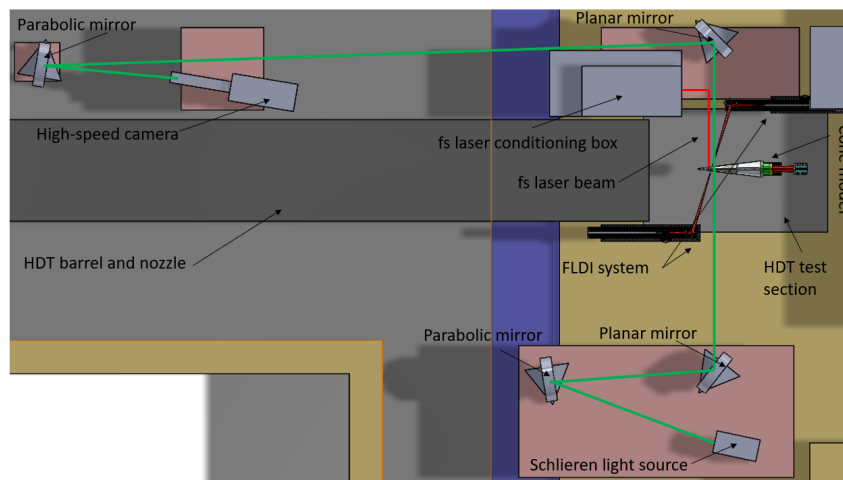**Fig 3.** Ultrafast laser beam path to HDT test section.

Fig 4. Schlieren arrangement.

Before initiating a test run, schlieren images were captured without hypersonic flow or energy deposition for each field of view. These preliminary images were used for subsequent background image subtraction for each acquired frame during post-processing. To enhance the distinction of pixel intensity variations near the boundary layer, the average image derived from images of the undisturbed flow, were also subtracted from the schlieren images [15, 16].

3.2. Focused Laser Differential Interferometry (FLDI)

FLDI is an advanced instrument renowned for its ability to detect density fluctuations with high sensitivity ($< 10^{-6} kg/m^3$), rapid response times (>10 MHz), and fine spatial resolution (typically encompassing a measurement volume of 0.1 x 0.1 x 20 mm). Details of FLDI theory are limited in this article for brevity, however, comprehensive insights into this instrument and its operational principles can be found in a publication by Ceruzzi and Cadou [17].
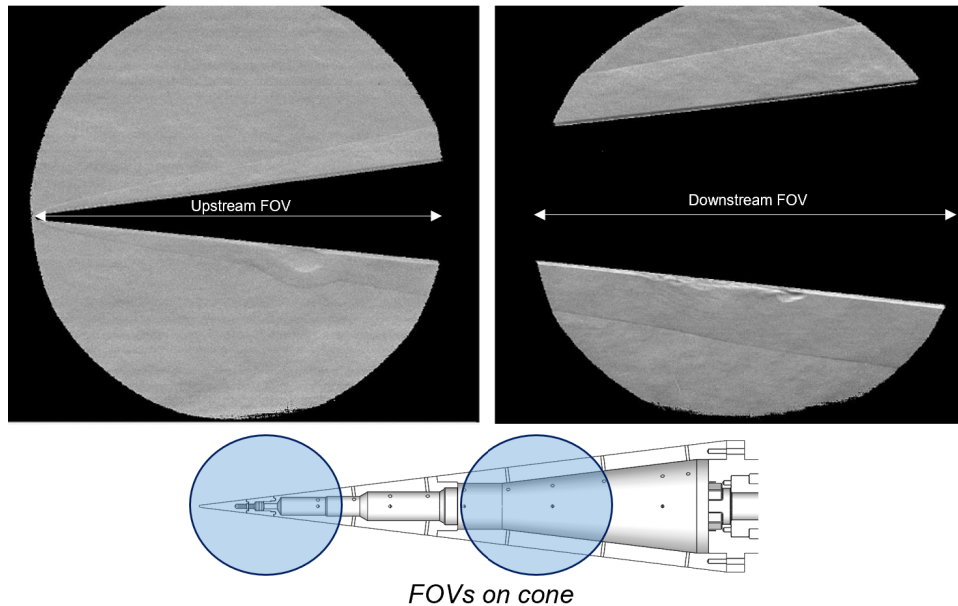
Fig 5. Schlieren imaging fields-of-view.

In essence, FLDI operates by directing two closely spaced, focused laser beams through the gaseous area of interest. Refractive index variations within the flow induce a phase difference between these two beams. As the beams are recombined beyond their focal point, the phase difference leads to interference, resulting in intensity fluctuations, which are recorded by a photodiode. Consequently, the voltage registered by the photodiode is directly proportional to the refractive index gradients within the flow. Gradients in the vicinity of the focal region exe rt a more pronounced influence than those situated farther from it, making FLDI largely insensitive to surrounding flow features outside the region of interest.In the context of this experiment, the FLDI employs a Laser Quantum Ventus solid-state continuous-wave laser with a wavelength (λ_0) of 671 nm. The laser beams are separated by Δx = 110 ± 5 μm, and the beam radius parameter at the focus (w_0) measures 5.6 ± 0.5 μm. Accurate determination of these latter two parameters was achieved through the use of a Thorlabs BC207VIS beam profiler camera.

Using the methods of Ceruzzi and Cadou in [17], the sensitivity of the FLDI, represented mathematically by the combination of transfer functions $H_{\Delta x}$ H_w, can be characterised using these three parameters, the focal spot separation, Δx, λ_0, and w_0. These parameters are plotted in the Figure 6 below against disturbance wavelength, λ_x, and distance from the focus (z). Figure 6 shows the instrument's sensitivity is maximised for disturbances with wavelengths of ≈ 220 μm. At these scales the instrument's depth of focus, defined as the full-width-half-maximum of the sensitivity, is ≈ 10 mm. For scales on the order of the boundary layer thickness on the model, $\lambda_x \approx 1.5$ mm, the depth of focus is ≈ 30 mm.

For the cone model in this work, the FLDI is position locations in the flow corresponding to the upstream and downstream positions of the schlieren field-of-view. When the schlieren is positioned upstream, visualising the nose of the cone, the FLDI focus is positioned ≈ 0.5 mm above PCB 3, downstream from the nose tip. When the schlieren is at the downstream position, the FLDI system is positioned just in front of PCB 8, with the focus again ≈ 0.5 mm above the surface of the cone. Typically, FLDI beams pass perpendicular to the flow direction, taking the shortest path across the test section. However, for these experiments, the FLDI beams are directed across the test section in a non-orthogonally, as illustrated in Figure 7, to interrogate a region of flow simultaneously with schlieren imaging, and did not adversely effect FLDI measurements. The schlieren light path traverses orthogonally across the test section (along the z-axis), thus the FLDI beam paths are positioned approximately 18° from the z-axis such that the optical components of both techniques do not interfere with one another.
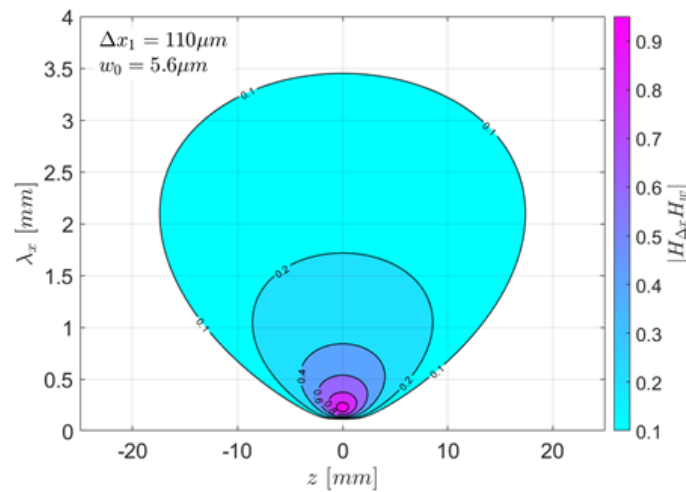
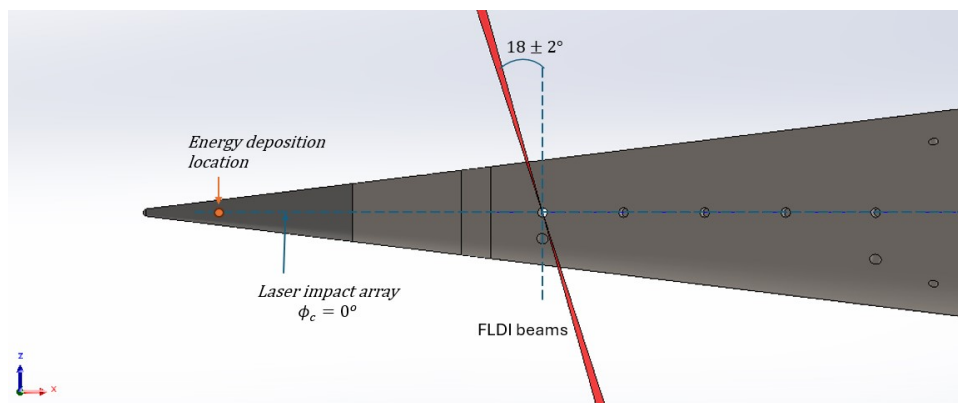**Fig 6.** FLDI sensitivity as a function of distance from focal point.

Fig 7. Non-orthogonal orientation and position of the FLDI beams relative the cone model.

3.3. Surface Measurements

PCBs 132A31 and 132B32 piezoelectric transducers were embedded within the model surface at discrete locations. For the purposes of this study, we exclusively focus on data obtained along the zeroth azimuth, as it offers a direct point of comparison with FLDI, which was situated beneath the cone model. The pressure transducers are connected to signal conditioners (PCB Piezotronics 482C), located externally from the test section, via shielded cabling, which runs internally through the model, sting, and then secured to D-SUB ports in the walls of the test section. The signals are digitised and recorded at 2 MHz using NI PXIe-6368 cards housed in a NI PXIE-1082 chassis. Voltages are converted to Pascals using supplier-provided calibration coefficients. The PCB signals were contaminated by several sources of noise. Noise from a Cavilux Cavitar laser (used to illuminate the schlieren images) appears as a high frequency signal (the Cavitar was pulsed at 1 MHz) present during a ≈ 400 µs period. Another noise signal appeared as periodic high-frequency bursts throughout the test time. To separate the useful signal from the noise, as well as investigate the frequency content of the flow features, continuous-wavelet-transforms (CWTs) were performed on the pressure signals to display frequency responses from PCB measurements and not pressure variation, due to corruption from signal noise. This is accomplished using MATLAB's cwt function with Morlet wavelets and 48 voices per octave. Only useful surface measurement data below a noise threshold are used for the proceeding analysis. For analysis of higher frequency content, we use the FLDI, which performs much better than PCBs at high frequencies.
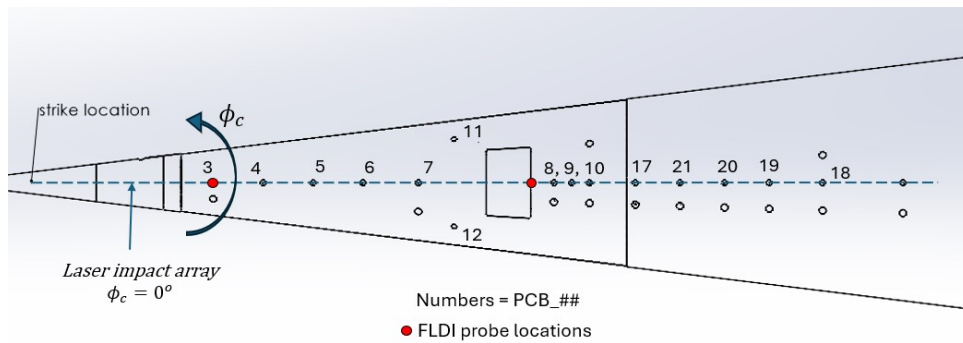
Fig 8. Cone model instrumentation and FLDI arrangement.

4. Results

4.1. Laser-Generated Flow Structures

Before presentation of results, it is beneficial to outline some nomenclature of the flow features that will be encountered henceforth. In general, this section will discuss and describe flow features seen in Figure 9, which include a spherical shock wave or blast wave dubbed a laser-generated shock (LGS), the hot-spot or hot core in the centre of the LGS, and turbulent wake disrupting the boundary layer.
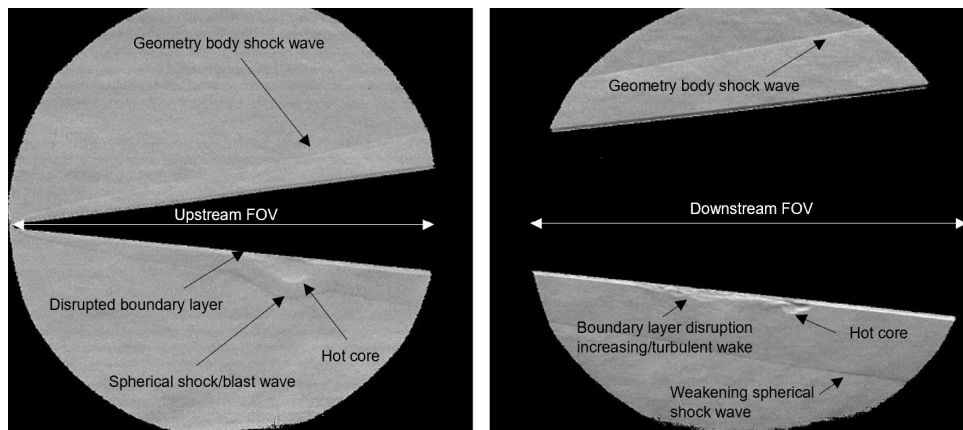
Fig 9. Flow structure nomenclature with reference to images taken from schlieren imagery.

4.1.1. Baseline conditions

All proceeding results are taken from baseline flow conditions and laser settings. These are a Mach 7 flow with a unit Reynolds number of $12.3 \pm 0.9 \times 10^6/m$, and a laser pulse energy of around 40-43 mJ (maximum energy) pulsed for a duration of 62.6 fs. This gives a point of comparison when a sweep through laminar to fully turbulent flow conditions are presented.

Figure 10 shows the visualised disturbed flow field along the zeroth azimuth of the cone at five instances in time after energy has been deposited into the boundary layer, where a spherical shock begins to form and propagate from the model surface. Following this, the shock continues to expand and a hot spot or hot core begins to form as a result of a short duration plasma. Proceeding further in time after the energy deposition, the hot spot encompasses the majority of the LGS volume. As the spherical shock expands further at the local speed of sound, the hot spot remains finite in size while entraining the boundary layer on its upstream side where the boundary layer is separated from the surface at the rear of the hot spot (upstream on the cone), which persists through the final schlieren image frame at the bottom of Figure 10.
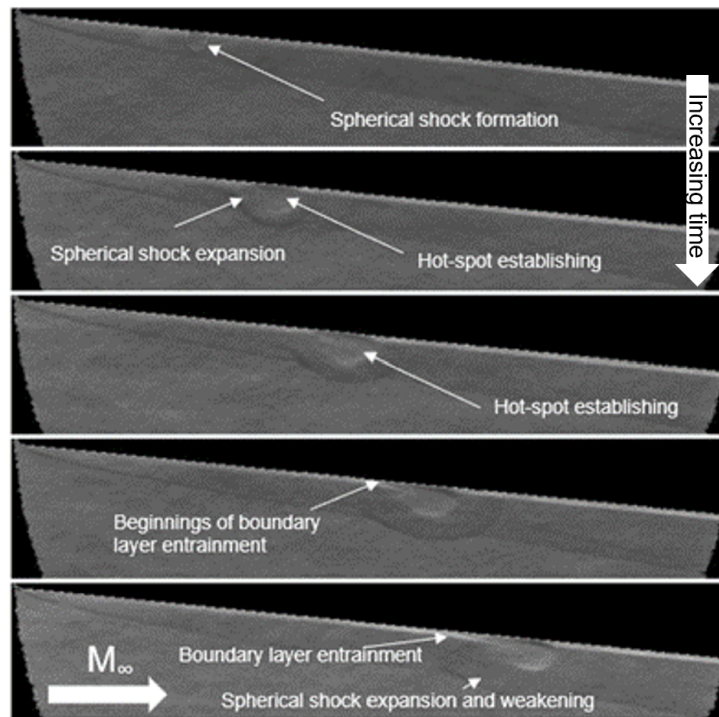
Fig 10. Schlieren imaging of upstream FOV of nominal flow condition and laser settings taken from Shot 3076.

Similarly, Figure 11 shows the flow effects of the LGS at baseline conditions downstream from the energy deposition position. The first schlieren image at the top of the figure, we can immediately see that the spherical shock wave has expanded significantly, and the hot-spot structure has evolved into an elliptical shape. The hot spot is advecting on top of the boundary layer with a portion entrained into its structure, again, looking to be detached from the model surface. As the LGS features travel downstream, the expansion of the spherical shock continues, and is seen to be interacting or distorting the cone body shock. Behind the hot spot, after the boundary layer has been separated from the surface, a turbulent wake region develops. This wake is disrupting the local boundary layer state, growing both in length and normal to the model surface.

Figure 12 shows FLDI data from the baseline conditions at the upstream FOV with respect to time, which provides a quantitative temporal measurement of LGS flow features. Firstly, an undisturbed laminar boundary layer is detected, which oscillates about 0 rads, effectively acting as a boundary layer state baseline. When the leading-edge of the LGS front passes through the FLDI we see a sharp spike above the zero-line, indicating a step change in density. This is followed by a large feature below the zero-line generated by the hot-spot. As the FLDI instrument is sensitive to density gradient, we can see that this large spike corresponds with a reduction in density, which implies an increase in temperature. This hot-spot feature is then followed by signal above the zero-line, inferring a density increase and decreasing temperature, as well as large amplitude fluctuations being evidence of instabilities and turbulence. This is then followed by the boundary layer re-establishing itself to the laminar state we saw prior to the LGS around 0 rads.

Figure 13 is a CWT spectrum of this data, where there is evidence of the three key LGS flow features. This CWT confirms the significance of the hot-spot disruption magnitude, being the brightest in the spectra, and shows the formation of second Mack mode instabilities, whose frequency matches that seen in Kerth et al. [18], are contained in or induce the turbulent wake seen in the schlieren images above.
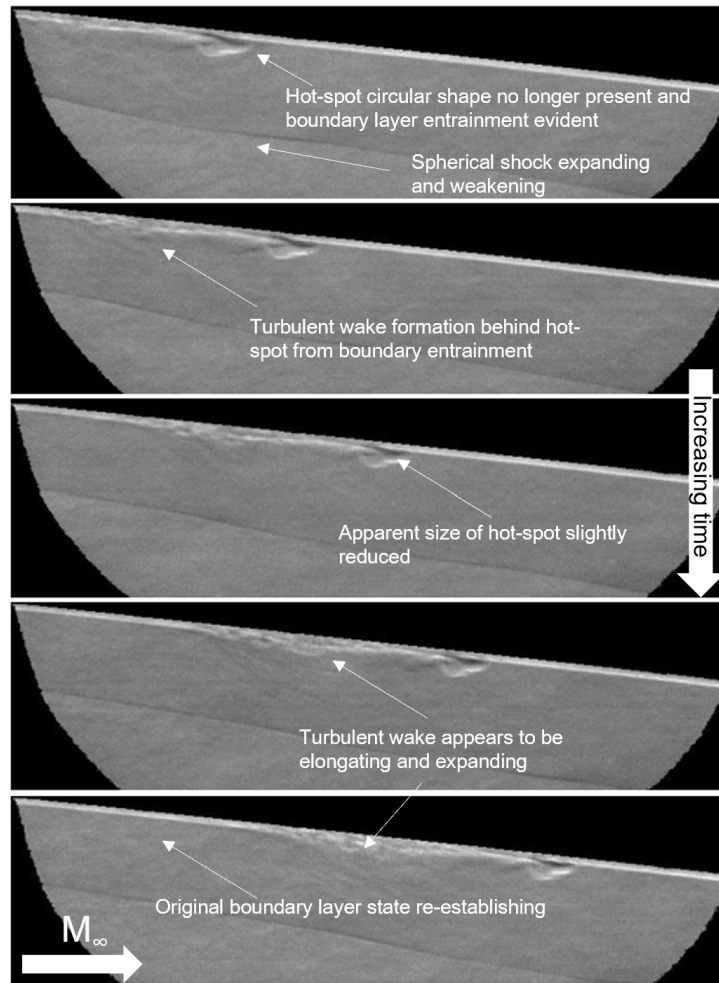
Fig 11. Schlieren imaging of downstream FOV of nominal flow condition and laser settings taken from Shot 3085.

Figure 14 shows CWT spectra for PCB data at 12 locations along the cone length. At x = 147mm, we see a singular disturbance from the more concentrated LGS, which is closer to the hot core. When looking downstream, at x = 175 to 203 mm, the individual hot spot and wake are becoming more spectrally, and spatially, segregated. As the LGS disturbance migrated further downstream at x = 231 to 358 mm, the individual features begin to amalgamate, as the trailing turbulent wake continues to expand and elongate with evidence of broadband turbulence seen at x = 459 to 489 mm.

Similarly to previously shown FLDI data, Figure 15 illustrates the FLDI data taken from the downstream position. Here we have the absence of the shock peak, as we do not see a singular spike above the zero-line before the first large negative spike. This agrees with what is observed in the schlieren imagery in the downstream FOV, with the LGS expanded and significantly weakened. However, we do see a less pronounced hot-spot spike, and a doubling in the turbulence magnitude and duration, the latter is further confirmed in the CWT spectra in Figure 16. Again, these both validate what is visually observed. Additionally, we see the existence of second mode instabilities after the turbulence has passed, meaning the boundary layer has not reverted to its laminar state.

4.2. Reynolds Number Sweep
The following results shows the effects of varying freestream Reynolds number on the studied flow field. Here, all laser parameters are held constant (62.6 fs, 43 mJ, 1 mm spot size) and the fill pressure of the
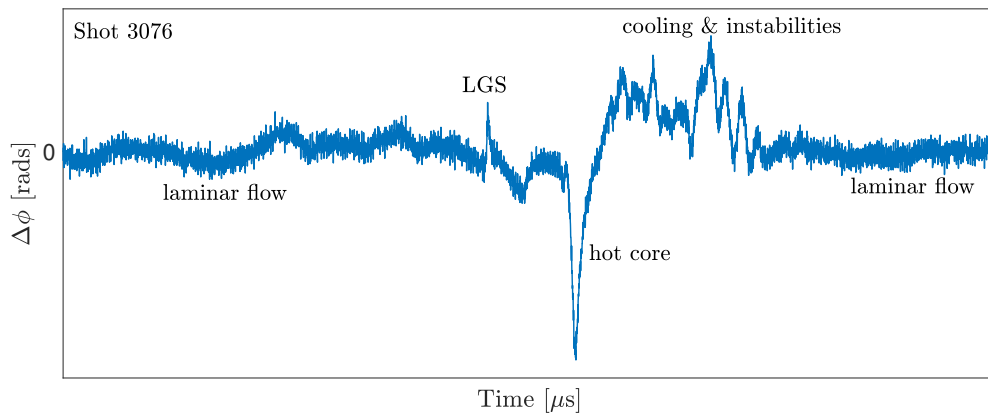
Fig 12. FLDI data showing LGS flow features passing over the upstream FLDI position.
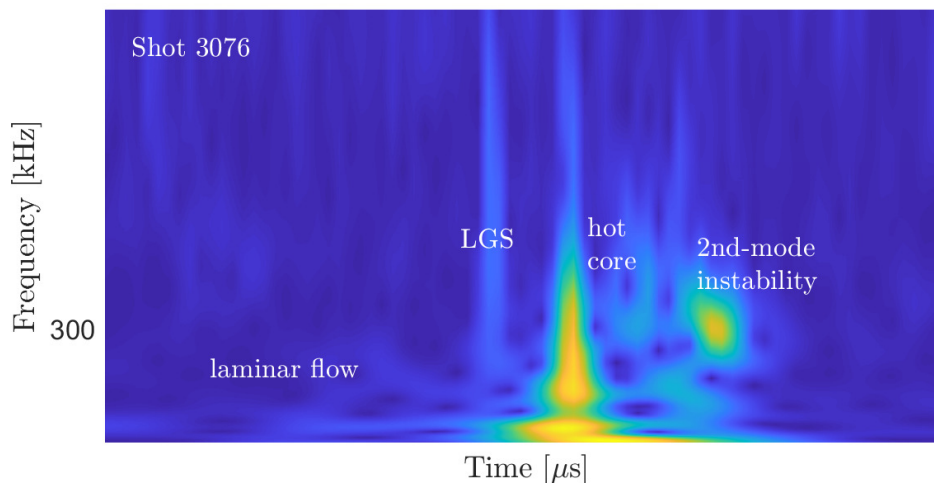

Fig 13. FLDI CWT of Shot 3076. Here it is easy to discern the frequency space disturbances from the boundary layer state from its original state. We see the three features, the shock, the disruption from the hot spot, and then the formation of the second mode instabilities.

facility is varied, causing changes in freestream pressure, and thus, changes in the freestream Reynolds number. Before looking at the effect of unit Reynolds number on the energy deposition interaction, it is worth noting effects on the flow field without energy deposition. As expected with an elevated unit Reynolds number, the transition to a turbulent boundary layer takes place farther upstream compared to the baseline scenario stated previous, where the transition occurs at x = 489 mm and x = 384 mm, respectively. This demonstrates that augmenting the unit Reynolds number results in a reduction of boundary layer stability.

When considering energy deposition with variation in unit Reynolds number, the magnitude of fluctuations seen in CWT scalograms of FLDI signals associated with the hot spot and post hot spot turbulence increase dramatically, indicating the magnitude of LGS feature appears dependant on unit Reynolds number. An increase in fluctuation amplitude is not unexpected, as increasing the Reynolds number is accomplished by increasing the mean density of the flow. This is equivalent to a density-based "turbulence intensity" often used in literature [19, 20]. The normalised fluctuations are plotted in Figure 17,
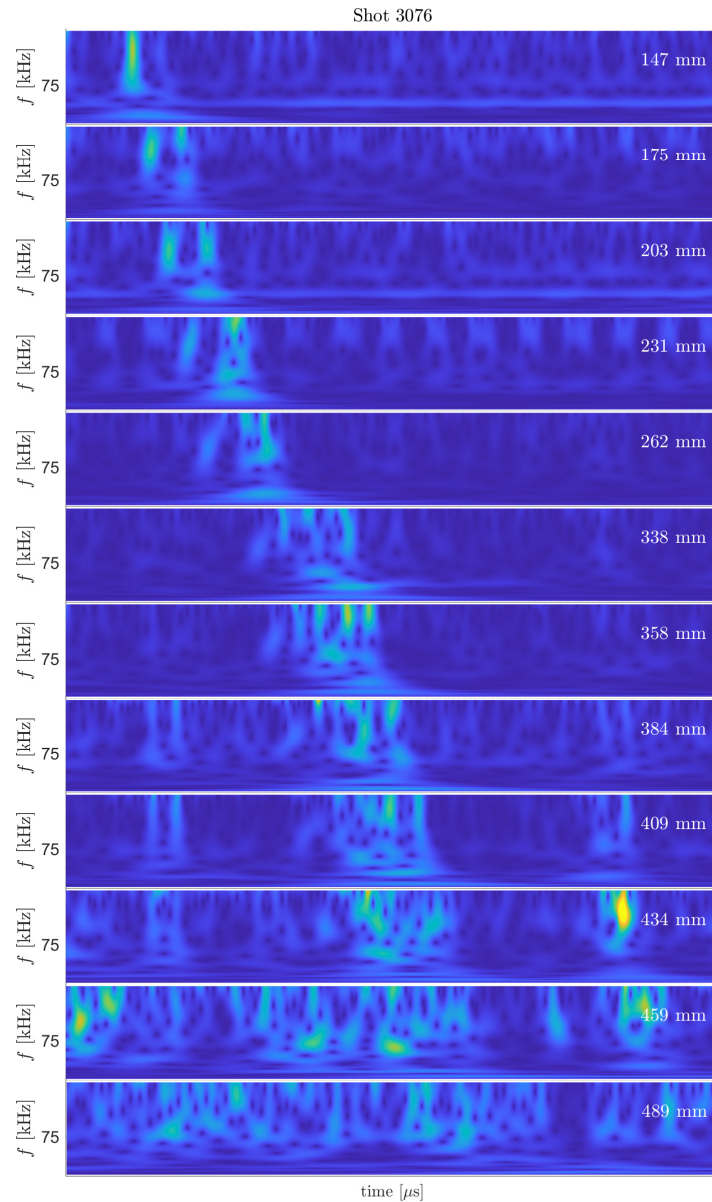
Fig 14. CWT of PCB data along the zeroth azimuth along the cone model for the nominal laser and flow conditions.

which shows that the normalised hot spot magnitude, appears independent of unit Reynolds number, while the post hot spot turbulence magnitude increases with unit Reynolds number. Essentially, the magnitude of the density gradient fluctuations associated with the hot spot scales linearly with unit Reynolds number, while the turbulence intensity increases non-linearly with unit Reynolds number for this upstream location.
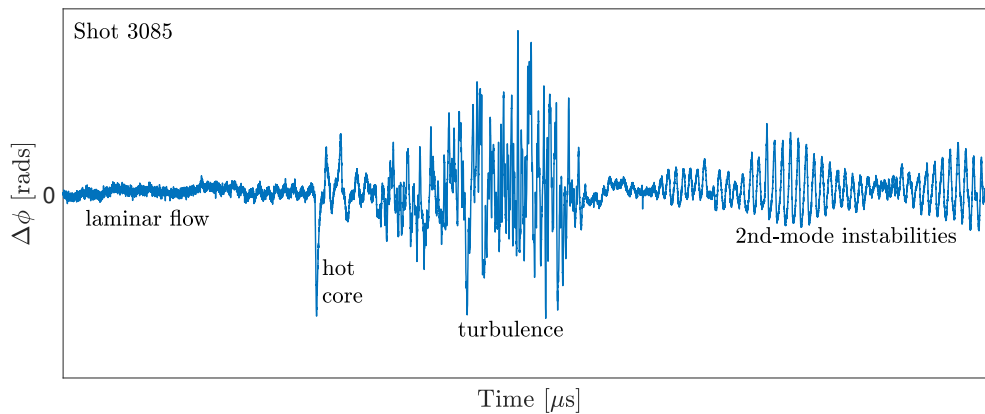
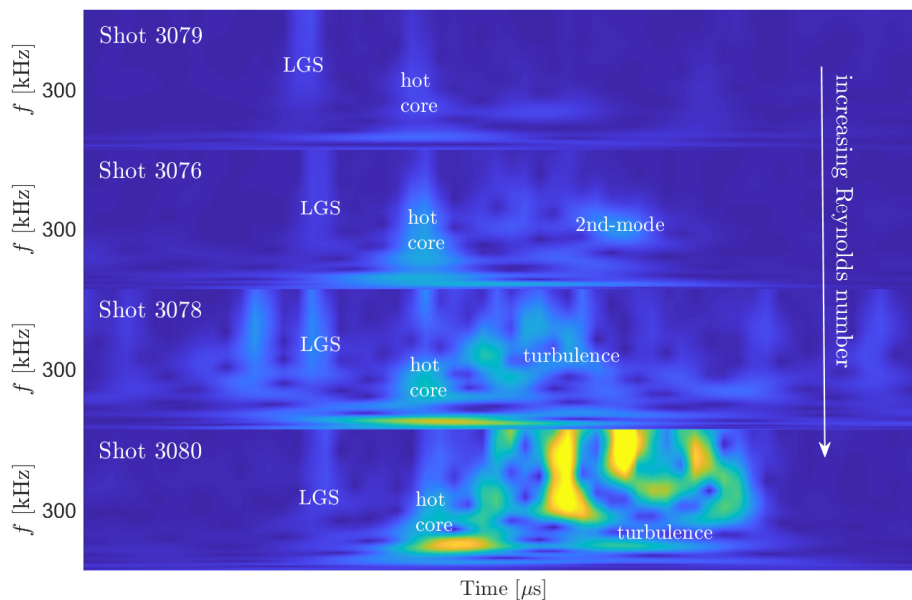**Fig 15.** FLDI data showing LGS flow features passing over the FLDI downstream measurement position.

Fig 16. CWT scalograms of FLDI signals associated with the hot spot and post hot spot turbulence increase dramatically for evaluated unit Reynolds numbers.

Figure 18 and Figure 19 show a set of time series schlieren images from the $Re_{unit} = 24.1 \times 10^6/m$ case for both the upstream and downstream FOVs, respectively. The features of the hot spot, shock, and turbulent wake appear with higher contrast, which is expected due to the higher mean density. Additionally, the hot spot size appears smaller than the baseline case plotted in Figure 10 and Figure 11.

FLDI data collected atnthe downstream locatio , for the four different unit Reynolds numbers, exhibited broadband fluctuations from that indicated the passing of the turbulent wake caused by energy deposition. The amplitude of this turbulent wake, as well as the frequency of second mode instabilities, in this instance at f ≈ 300 kHz, increases with Reynolds number. Figure 20 illustrates that the turbulence intensity of the turbulent wake region does not increase much above $Re_{unit} = 5.7 \times 10^6/m$ (top sub-
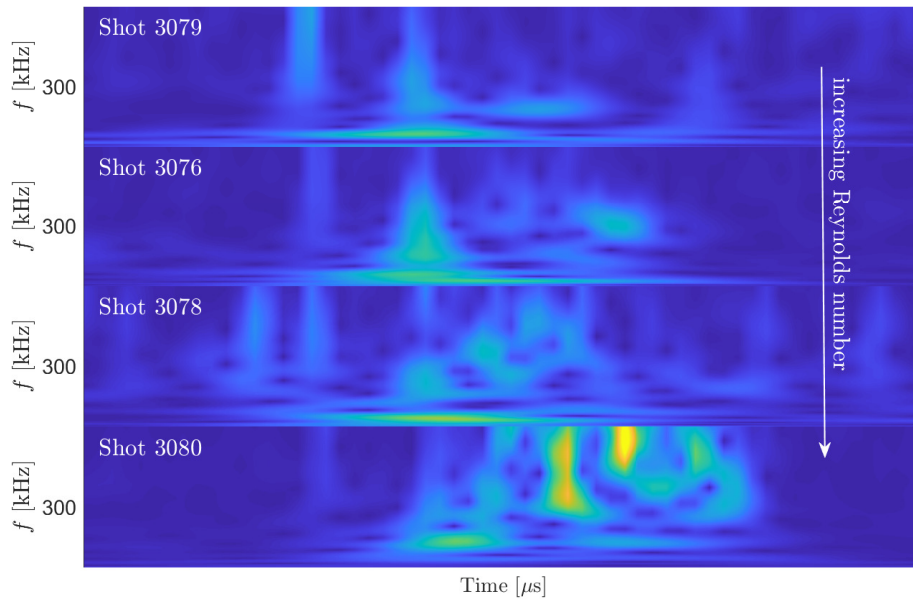
Fig 17. CWT spectra of FLDI data at the upstream location showing the increase in turbulence magnitude, which has been normalised by the baseline unit Reynolds number.
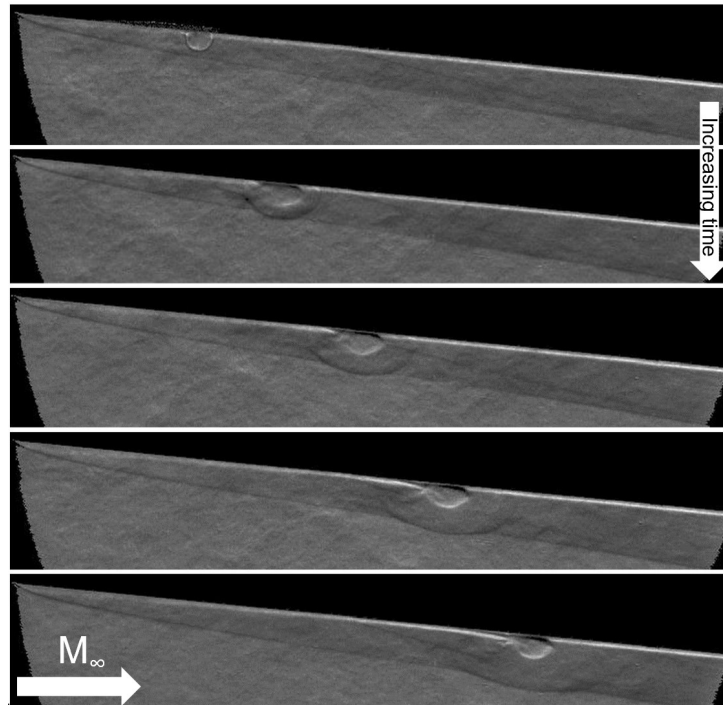

Fig 18. Upstream FOV of the high unit Reynolds number test ($Re_{unit} = 24.1 \times 10^6 / m$). Note the improved contrast flow features and increased shock strength.
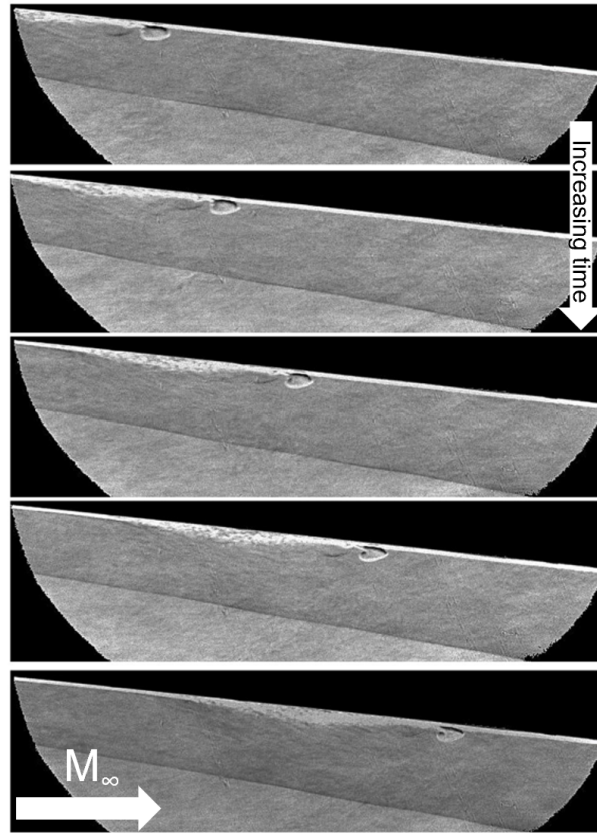
Fig 19. Downstream FOV of the high unit Reynolds number test ($Re_{unit} = 24.1{\times}10^6/m$).

figure). Figure 20 also suggests a slight increase in the duration of the turbulent wake with Reynolds number. To decouple the results from this effect, the FLDI signal is normalised by unit Reynolds number by dividing phase difference by the ratio between current and baseline unit Reynolds number. Thus, the signal from nominal case, $Re_{unit} = 12.3{\times}10^6/m$, is unaltered while larger or smaller Reynolds number cases have decreased or increased amplitudes, respectively. To investigate this further, the turbulent wake length was manually tracked from schlieren images at three instances in time from downstream FOV and plotted in Figure 21. This figure illustrates a clear relative increase in turbulent wake length with unit Reynolds number. This result is likely explained by the decrease in boundary layer stability with increasing unit Reynolds number.
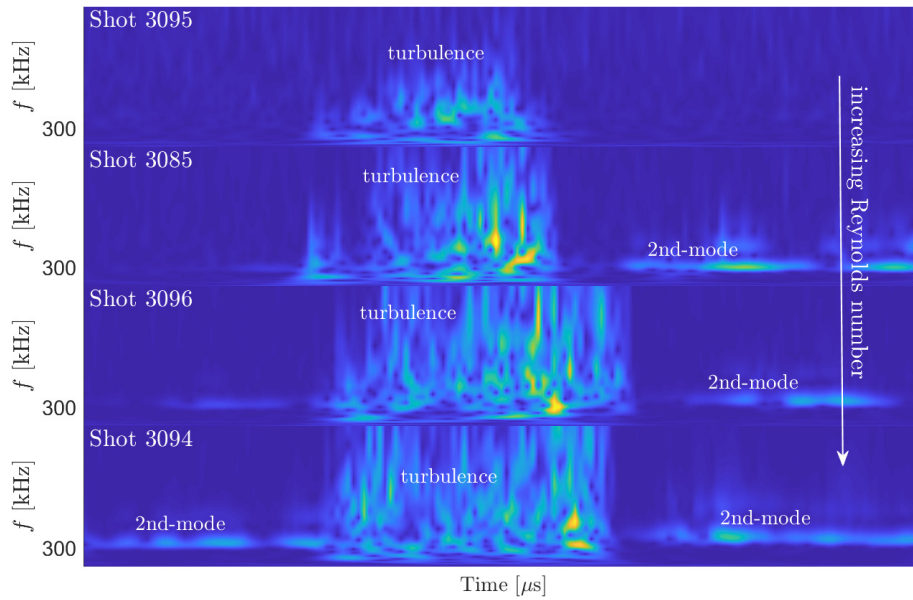
Fig 20. Comparison of FLDI CWTs collected at the downstream location at four different unit Reynolds numbers.
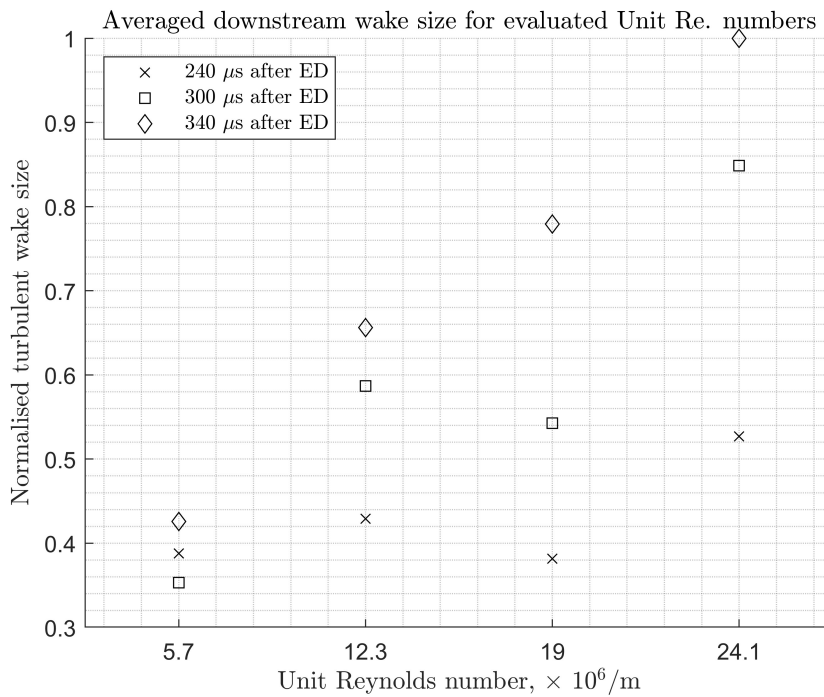

Fig 21. Averaged downstream wake length for the evaluated unit Reynolds number.

5. Conclusions

This paper presented results of a preliminary and fundamental study to evaluate boundary layer characteristics arising from optical energy deposition near the tip of a 7° half-angle axisymmetric cone in the Oxford High Density Tunnel (HDT) facility. An ultrafast Ti:Sapphire laser was used for energy deposition, that provided temporally precise, and synchronous delivery, of a single tightly focussed laser pulse to the target location. This investigation independently assessed the impact of the freestream unit Reynolds number variation on the disturbed boundary layer, which was independently evaluated across laminar to turbulent conditions, constrained by the extremal unit Reynolds numbers of 5.7 and $24.1 \pm 0.9 \times 10^6/m$, with laser energy and pulse duration held constant. For all tests, the boundary layer state was qualitatively and quantitatively characterised using high-speed schlieren imagery, FLDI, and surface-mounted high-frequency bandwidth pressure sensors. Flow features of the disturbed boundary layer that advected downstream after energy deposition, included the formation of a spherical shock wave that expanded radially and decayed, an elliptical high-temperature 'hot spot' region, and a trailing turbulent wake. The hot spot and turbulent wake density gradients increased linearly with unit Reynolds number, suggesting a local mean density or pressure relationship. Normalisation of these values using the mean density gave estimates of turbulence intensity, which appeared independent of unit Reynolds number. The hot spot size decreased with unit Reynolds number, which is could be caused by the higher mean pressure compressing the hot spot. The increasing instability of the boundary layer with unit Reynolds number led to longer duration turbulent wakes before the laminar boundary layer re-establishes. Future work will involve a direct comparison to data generated using a ns laser pulse duration for optical energy deposition into a hypervelocity boundary layer.

References

[1] Knight, D., Kuchinskiy, V., Kuranov, A., Sheikin, E.: Survey of aerodynamic flow control at high speed using energy deposition. 41st Aerospace Sciences Meeting and Exhibit, p. 525 (2003)

[2] Miles, R., Macheret, S., Martinelli, L., Murray, R., Shneider, M., Ionikh, Y., Kline, J., Fox, J.: Plasma control of shock waves in aerodynamics and sonic boom mitigation. 32nd AIAA Plasmadynamics and Lasers Conference, p. 3062 (2001)

[3] Knight, D.D.: Energy deposition for high-speed flow control. Cambridge University Press, Cambridge (2019)

[4] Brovkin, V., Afanas'ev, S., Khmara, D., Kolesnichenko, Y.: Experimental Investigation of Combined Laser-DC-MW Discharges. 44th AIAA Aerospace Sciences Meeting and Exhibit, p. 1459 (2006)

[5] Cremers, D.A., Radziemski, L.J.: Handbook of laser-induced breakdown spectroscopy. John Wiley & Sons (2013)

[6] Starikovskiy, A.Y., Aleksandrov, N.: Gasdynamic flow control by ultrafast local heating in a strongly nonequilibrium pulsed plasma. Plasma Physics Reports, 47:148–209 (2021)

[7] Klimov, A., Koblov, A., Mishin, G., Serov, Y.L., Yavor, I.: Shock wave propagation in a glow discharge. Sov. Tech. Phys. Lett.(Engl. Transl.);(United States), 8(4) (1982)

[8] Aleksandrov, N.L., Bodrov, S.B., Tsarev, M.V., Murzanev, A.A., Sergeev, Y.A., Malkov, Y.A., Stepanov, A.N.: Decay of femtosecond laser-induced plasma filaments in air, nitrogen, and argon for atmospheric and subatmospheric pressures. Phys. Rev. E, 94:013204 (2016). URL http://dx.doi.org/10.1103/PhysRevE.94.013204

[9] Oliveira, A.C., Minucci, M., Toro, P., Chanes Jr, J., Myrabo, L., Nagamatsu, H.: Bow shock wave mitigation by laser-plasma energy addition in hypersonic flow. Journal of Spacecraft and Rockets, 45(5):921–927 (2008)

[10] Yang, L., Erdem, E., Zare-Behtash, H., Kontis, K.: Single pulse laser energy deposition in quiescent air and hypersonic flows. 18th AIAA/3AF International Space Planes and Hypersonic Systems and Technologies Conference, p. 5870. Tours, France (2012)

[11] Gnemmi, P., Charon, R., Dupéroux, J.P., George, A.: Feasibility study for steering a supersonic projectile by a plasma actuator. AIAA Journal, 46(6):1308–1317 (2008)

[12] Wylie, S., Doherty, L., McGilvray, M.: Commissioning of the Oxford high density tunnel (HDT) for boundary layer instability measurements at Mach 7. 2018 Fluid Dynamics Conference, p. 3074 (2018)

[13] McGilvray, M., Doherty, L.J., Neely, A.J., Pearce, R., Ireland, P.: The Oxford High Density Tunnel. 20th AIAA International Space Planes and Hypersonic Systems and Technologies Conference. American Institute of Aeronautics and Astronautics (2015). URL http://dx.doi.org/10.2514/6.2015-3548

[14] Wylie, S.: Hypersonic boundary layer instability measurements at low and high angles of attack. Ph.D. thesis, University of Oxford (2020)

[15] Versluis, M.: High-speed imaging in fluids. Experiments in fluids, 54:1–35 (2013)

[16] Settles, G.S., Hargather, M.J.: A review of recent developments in schlieren and shadowgraph techniques. Measurement Science and Technology, 28(4):042001 (2017)

[17] Ceruzzi, A.P., Cadou, C.P.: Interpreting single-point and two-point focused laser differential interferometry in a turbulent jet. Experiments in Fluids, 63(7):112 (2022). URL http://dx.doi.org/10.1007/s00348-022-03459-w

[18] Kerth, P., Le Page, L.M., Wylie, S., Ravichandran, R., Ceruzzi, A., Williams, B.A., McGilvray, M.: Displacement of hypersonic boundary layer instability and turbulence through transpiration cooling. Physics of Fluids, 36(3) (2024)

[19] Ceruzzi, A., Callis, B., Weber, D., Cadou, C.P.: Application of focused laser differential interferometry (FLDI) in a supersonic boundary layer. AIAA SciTech Conference, p. 1973 (2020)

[20] Settles, G.S., Fulghum, M.R.: The focusing laser differential interferometer, an instrument for localized turbulence measurements in refractive flows. Journal of Fluids Engineering, 138(10):101402 (2016)